Scanning acoustic microscopy investigation of weld lines in injection-molded parts manufactured from industrial thermoplastic polymer

Esam T. Ahmed Mohamed[a,*], Min Zhai[a,b], G. Schneider[d], R. Kalmar[d], M. Fendler[d], Alexandre Locquet[a,b], D.S. Citrin[a,b], N.F. Declercq[a,c]

[a] Georgia Tech-CNRS UMI2958, Georgia Tech Lorraine, 2 Rue Marconi, 57070 Metz, France
[b] School of Electrical and Computer Engineering, Georgia Institute of Technology, Atlanta, Georgia 30332-0250 USA
[c] School of Mechanical Engineering, Georgia Institute of Technology, Atlanta, Georgia 30332 USA
[d] CEA Tech 5 Rue Marconi, Bâtiment Austrasie, 57070 Metz, France

ARTICLE INFO

ABSTRACT

Scanning acoustic microscopy (SAM) is used to characterize welds in a thermoplastic polymer (ABS) manufactured by injection-molding, particularly at the locations of weld-lines known to form as unavoidable significant defects. Acoustic micrographs obtained at 420 MHz clearly resolve the weld lines with morphological deformations and microelastic heterogenity. This is also where terahertz (THz) measurements, carried out in support of the SAM study, reveal enhanced birefringence corresponding to the location of these lines enabling verification of the SAM results. Rayleigh surface acoustic waves (RSAW), quantified by $V(z)$ curves (with defocusing distance of 85 μm), are found to propagate slower in regions close to the weld lines than in regions distant from these lines. The discrepancy of about 100 m/s in the velocity of RSAW indicates a large variation in the micro-elastic properties between areas close to and distant from the weld lines. The spatial variations in velocity (V_R) of RSAWs indicate anisotropic propagation of the differently polarized ultrasonic waves.

1. Introduction

Ulrasound and terahertz (THz) imaging provide access to the mechanical and optical properties of materials, thus giving complementary information. The current study applies ultrasound, specifically scanning acoustic microscopy (SAM) to obtain quantitative information concerning mechanical properties related to injection-mold weld lines in a commercial ABS electrical receptical plate, while THz imaging is applied to map the birefringence and is used to verify the SAM results.

Injection molding is one of the most widely used mass-production of manufactured polymers. It is an attractive process because of its versatility in forming various shapes with high degree of complexities (Mistretta et al., 2018; Chen and Turng, 2005). In injection molding, the plastic polymer is subjected to a multi-phase process including heating, plasticizing, pressurizing, and infusion to the mold. Many parameters associated with the various process steps are involved (Chen and Turng, 2005), including melt processing temperature, mold temperature, injection flow rate, and holding pressure (Bociaga, 2000; Heidari et al., 2019). The polymer is therefore subjected to a set of thermomechanical conditions, which result in modification of its intrinsic properties (Fu et al., 2005; Rizvi, 2017). As a result of the multi-step process, changes

in the strength and consequently morphological and structural variations take place (Mohan et al., 2017). The large pressure variations, for instance, were reported to be substantially influential on the shrinkage and warpage of the product (SJ et al., 2004). Ultrasound tomography investigations indicate fast solidification and isotropic or anisotropic shrinkage accompanied by warpage, depending on conditions. The solidification and changes in volume and structure were attributed to the large difference between melt temperature and mould temperature followed by a freezing phase, leading to the occurrence of internal (residual) stresses (Mohan et al., 2017; Hopmann and Wipperfürth, 2017).

Changes in morphology as manifested by formation of crystalline phases were found not to have a significant effect on the elastic properties (Ghosh et al., 2007). However, during the process, line welds (or knit lines) unavoidably form during the recombination, when two or more flow fronts meet in the cavity during injection moulding (Agassant and Mackley, 2016). Welds comprise points of weak mechanical properties (Nasić et al., 2018). They are also known to have an altered optical refractive index (Oh et al., 2018).

The sample investigated here, is a commercially purchased electrical receptacle plate made up by injection molding of the

---

thermoplastic polymer Acrylonitrile butadiene styrene (ABS). ABS are thermos-copolymers with styrene and acrylonitrile constituting the matrix and polybutadiene or a butadiene elastomers dispersed as a grafted particulate phase, known to be highly adaptable and suitable for injection molding (Kulich et al., 2002).

While SAM is sensitive to the variations in the mechanical and visco-elastic properties at microscopic scales, THz imaging is sensitive to the optical properties at wavelengths between a few tens to hunders of microns. SAM has been employed in the evaluation of molded plastic electronic components to detect defects such as voids, delaminations, and cracks, where water ingress (displacement of air that fills defect-generated cavities by water molecules) was studied (Benak, 2019). SAM also faciltated the inspection of the microstructural detailed analysis of weld joints and the detection of defects, such as nugget failures. Tittmann et al. (Tittmann and Kessler, 2018) elaborate the use of a combination of various SAM-based techniques and report on the high efficiency of such approaches for these purposes.

1.1. Terahertz birefringence imaging of weld lines

THz imaging was carried out to verify the SAM results. We use a pulsed, broadband THz time-domain system (TeraView Ltd, TPS Spectra 3000) (Dong et al., 2017). THz imaging is performed in near normal incidence reflection mode. The sample is raster-scanned by a set of motorized stages moving in the x- and y-directions with transverse step size of 200 μm which is also roughly the transverse resolution of the system. We first carry out reflective experiments disregarding polarization. The arrival time at the detector of the THz pulse reflected from the top air/ABS interface provides a way to image the surface morphology on the tens-of-microns scale. Our second set of experiments employed polarization-resolved imaging. A knowledge of the sample thickness (measured by calipers) and the time delay between the reflected THz pulse from the top air/ABS interface and from the bottom ABS/air interface provides the refractive index for the given polarization.

1.2. Reflection SAM: Modus operandi and contrast mechanisms

Reflection SAM utilizes a focusing piezoelectric transducer that receives a short RF pulse (duration ~ 10 − 30 ns) and converts it into mechanical (acoustic) waves. The acoustic waves propagate through the lens body (Fig. 1) and are focused sharply by the spherical cavity of the lens into a diffraction limited point at the interface between a coupling fluid and the sample. Reflection occurs when a mismatch in the acoustic impedance is realized at interfaces (Demirkan et al., 2020). For normal incidence, it is the product of the mechanical density and velocity of ultrasound. The reflected signal is received by the transducer and is converted into an electric signal. An image is then formed by

Fig. 1. The principle of SAM and the defocusing to collect the V(z).

scanning in two dimensions and processing the reflected signal into a greyscale map.

The bulk and shear moduli of elasticity are related to the velocity of propagation of longitudinal and shear ultrasonic waves, respectively. The velocity of surface acoustic waves (SAW) is related to both compression and shear moduli of rigidity (Yu and Boseck, 1995). The attenuation of the acoustic signal passing through the inspected object is related to the viscous properties of the sample in addition to scattering. The spatial variations in the mico-viso-elastic properties, thus, comprise a major contribution to the contrast in SAM. The contrasts are also considerably influenced by the topography, thickness, interferences, and the variations of the reflected signal with the defocus distance of the transducer.

1.3. Variation of the reflected signal with the defocus distance of the transducer V(z)

A specific feature of SAM is that imaging contrast varies considerably with the distance between the acoustic lens and the specimen. This enables the visualization of subsurface regions depending on the acoustic properties of the specimen (Gremaud, 2001; Ahmed Mohamed and Declercq, 2020) and the numerical aperture (opening angle) of the acoustic lens. The ray model illustrated in Fig. 1 provides a simplified view of the excitation and detection of RSAW by defocusing the acoustic lens towards the sample. Acoustic waves incident at the Rayleigh critical angle (ray 1), excite Rayleigh surface acoustic waves (rays 3) that propagate along a path symmetrical to the exciting rays to the transducer. Rayleigh waves can be excited and detected by appropriate defocusing utilizing an acoustic lens with a sufficiently large aperture that exceeds the critical angle for exciting Rayleigh waves. RSAWs propagate along the surface of the sample and leak energy back into the couplant and thus, excite a compressional wave in the fluid under the Rayleigh angle. The echoes of these compressional waves interfere with the specularly reflected waves (ray 2). The voltage value of the resulting (rectified and integrated) complex signal depends sensitively on the lens-to-sample distance (z) and the wavelengths in the couplant. As the axial spacing between the acoustic lens and the sample surface z changes, the relative phases of the interfering waves vary, so that the superposition alternates between constructive and destructive interference. This effect considerably contributes to the contrast in the acoustic micrographs. A plot over the defocus results in an interference pattern referred to as the V(z) curve containing minima and maxima according to the interference of the two wave modes (Weiglein and Wilson, 1978). The period of the resulting oscillations Δz, in the V(z) curve, can be calculated from the phase relations and forms the basis for calculating the velocity of the RSAWs in the sample surface. Eq. (1) gives V(z) in terms of the sample and system parameters as (da Fonseca et al., 1993).

$$V(z) = 2\pi \int_0^{\frac{\pi}{2}} P^2(\theta) R(\theta) exp[-i2kz\cos\theta] \cos\theta \sin\theta d\theta \qquad (1)$$

where $P(\theta)$ is the pupil function that expresses the angular emission and detection properties of the acoustic lens and θ is the incidence angle. The integral above considers the overall geometrical incident waves with incidence angles that range from 0° to the half opening of the semi-aperture θ_{SA}, $R(\theta)$ is the reflectance function describing the amplitude and the phase of reflected waves as a function of the incident angle θ, and k is the propagation constant, $k = \frac{2\pi f}{v}$, with f the acoustic frequency and v the velocity of propagation of acoustic waves in the coupling fluid. In addition, we have

$$\Delta z = \frac{\lambda_0}{2(1 - \cos\theta_R)} \qquad (2)$$

where, $\Delta\Delta z$ is the periodicity of the oscillations in the V(z) curve, λ_0 is the wavelength of the acoustic waves during propagation in the couplant, and λ_R is the Rayleigh critical angle.
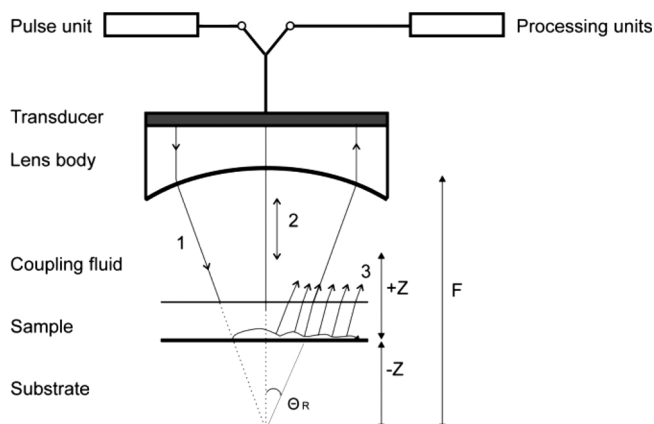
The velocity of propagation of the Rayleigh surface acoustic waves V_R can be expressed in terms of the ratio to the critical angle θ_R as

$$V_R = \frac{V_0}{\sin\theta_R} \qquad (3)$$

The value of V_R is related to shear wave velocity of the material V_S as (Briggs, 1992)

$$\frac{X^3}{8(1-X)} + X = \frac{1}{1-\sigma}$$

where, $X = (V_R)^2/(V_S)^2$ and σ is Possion's ratio.

2. Results and discussion

To inspect the micro-elastic features of the welded sample, high-resolution acoustic micrographs were taken at various positions on the surface of the sample and subsurface imaging was performed for regions close to the weld lines. The SAM used (ELSAM, Ernst-Leitz Scanning Acoustic Microscope; PVA TePla Analytical Systems, GMBH, Westhausen, Germany) allows imaging at frequencies f that range from 400 MHz to 1.2 GHz. A focusing transducer operating at a center frequency of 420 MHz was utilized.

Fig. 2 shows an optical camera image of the investigated plate, with the specified area A, on the front side. This is a commercially produced ABS electrical receptical plate. The weld line runs horizonatally through the plate and its location is indicated by the red arrows. The weld line is not visible to the eye. We present results for region A shown in the figure.

The acoustic micrograph in Fig. 3 is acquired in region A shown in Fig. 1. Fig. 3(a) shows a weld line forming a trough-like structure in an elevated region (of about 120 μm above the surface of the sample) at the location of the weld. Fig. 3(b) shows the adjacent flat part of the sample, 1500 μm a part of the weld line.

The confocal nature of SAM allows the pointwise insonifying and detection of reflection of ultrasound at interfaces between media of different acoustic impedances. Images are formed from the magnitude of the detected signal in a C-scan and represented as a greyscale. The contrast of focused images (performed with the focal distance adjusted to the surface of the sample) originates from the variations in the acousto-mechanical properties, mainly the mechanical density and the micro-elasticity, interferences and from wave mode conversions. Acoustic attenuation (viscous losses and scattering) also contribute to image contrast. A considerable source of contrast is, however, in addition obtained by defocusing, during subsurface imaging.

A closer look into the microstructure was performed by imaging a smaller field of view (500 μm x 500 μm), 2 mm right and 3.5 mm left to the weld line, as shown in Fig. 4a and Fig. 4b, respectively. While the morphological and topographical variations are clearly obvious in the images in Fig. 3, the strong contrast in Fig. 4 indicates considerable
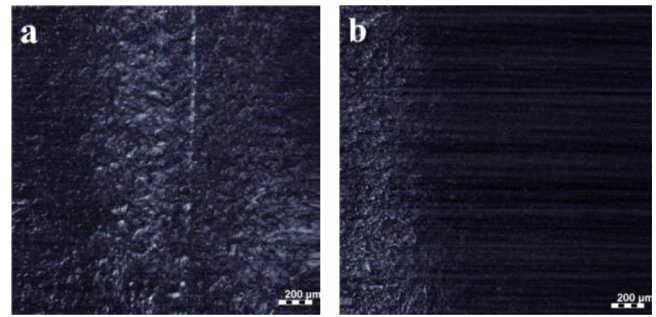

Fig. 3. SAM micrographs imaged at $f = 420$ MHz **a)** The weld line and a surrounding elevated area in region A in Fig. 2 and **b)** The flat area 400 μm left to the weld line.
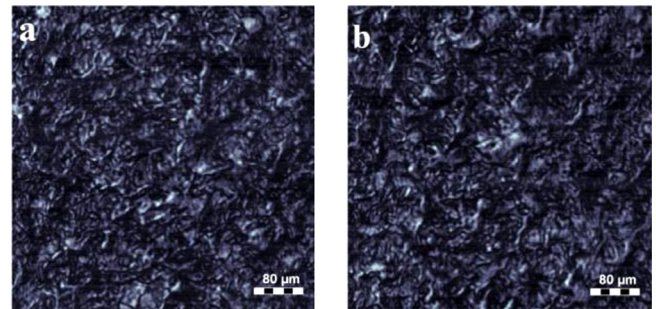

Fig. 4. In-focus acoustic micrographs in part A in Fig. 2 imaged at $f = 420$ MHz as a representative of the stack of images used to generate the V(z) curves. **a)** 2 mm left to the weld line **b)** 3.5 mm left to the weld line.

variations in the micro-elastic properties. The spatially variable strength of the reflected signal indicates variations in the acoustic impedances. The variations in the acoustic impedances may be attributed to corresponding variations in the microelastic moduli, resulting in a spatially varying acoustic propagation velocity and mode conversion. Variations in the mechanical density could also contribute to the mismatch in the acoustic impedance, in addition to viscous losses, as the received echoes traverse regions over which the extinction coefficients vary (Passini et al., 2011). A stack of images was taken by scanning in C-mode (in two dimensions), while translating the acoustic lens in the axial (orthogonal) direction (regarded as z-direction). Scanning was started slightly further from the focal plane and moving stepwise, passing through the focal region toward the sample (z in Fig. 1). More steps of scanning were performed in the z-direction (subsurface imaging), where the corresponding $V(z)$ curves carry the information about the surface acoustic waves (SAW) and their interferences. The stack of images in each measurement lasts about 8 min with the current technology. The $V(z)$ curves generated for the areas within the sample as shown in Fig. 5(a) and Fig. 6(a), are depicted in Fig. 5(b) and Fig. 6(b). The spacing distances Δz were calculated and the Rayleigh angle as well as the velocity of propagation of RSAW, V_R were computed as indicated in Table 1.

The closest area to the weld line that is flat permitting acquisition of $V(z)$ curves was 2 mm from the line, as shown in Fig. 3(a). The average velocities of Rayleigh surface acoustic waves (V_R) were computed using Eqs. (2) and (3) to be 1535 ± 27 m/s. V_R corresponding to $V(z)$ curves generated for the flat area 3.5 mm to the left of the weld line have an average value of 1624 ± 29 m/s. V_R is related to the velocity of the shear and compressional waves propagating in isotropic samples for the same Possion's ratio (Briggs, 1992; Li and Feng, 2016). Therefore slower V_R in regions closer to the weld lines indicate lower compression and shear moduli and consequently lower Young's modulus than regions located within further distances (Ahmed Mohamed et al., 2018). These findings are consistent with reported low rigidity near weld lines.
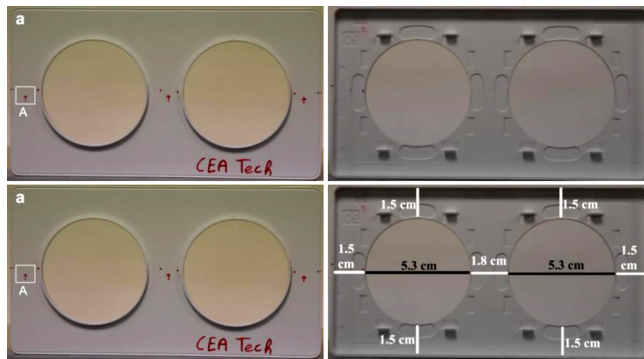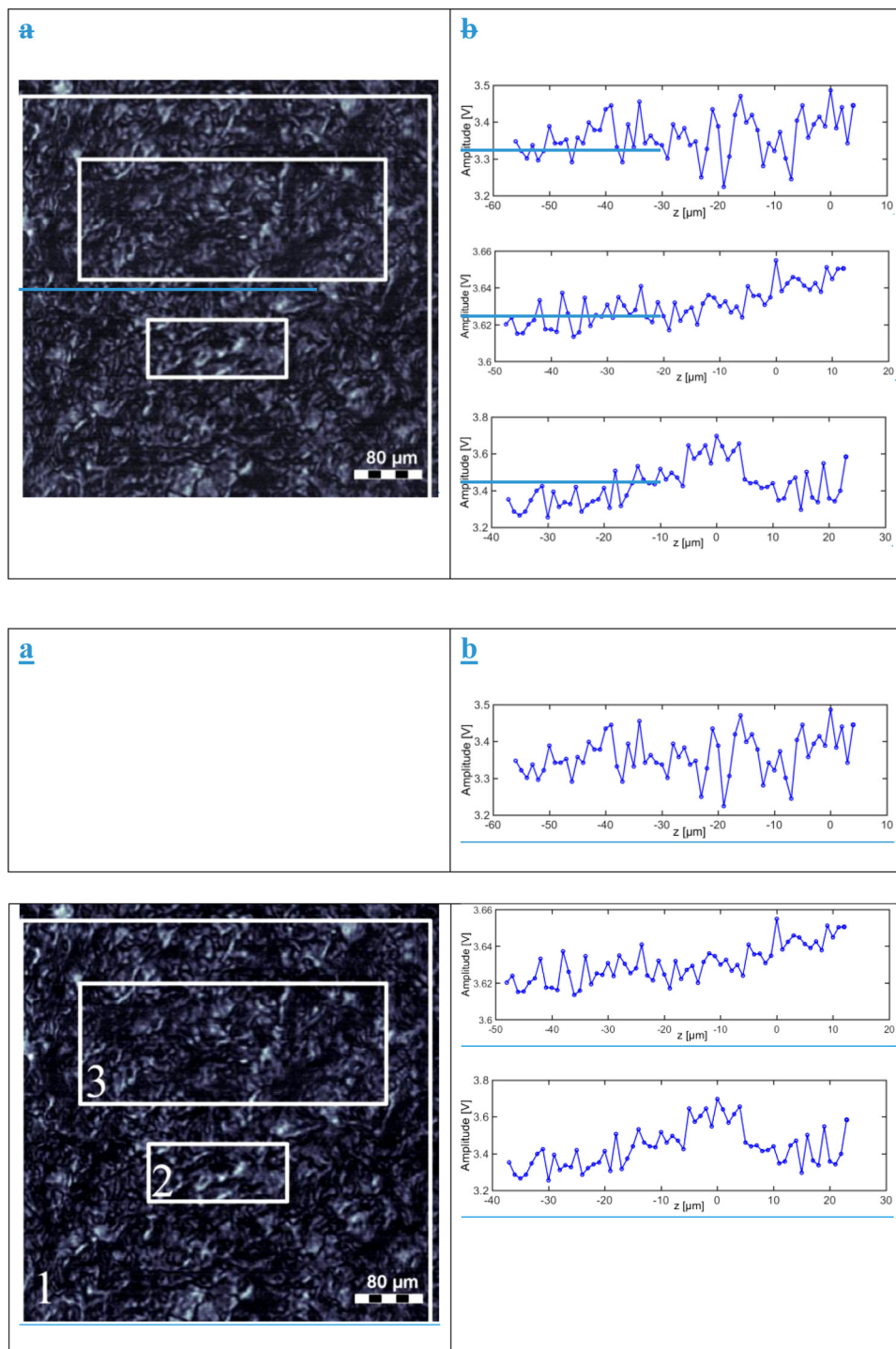

Fig. 2. Photograph of the ABS electrical receptical plate (15.4 cm x 8.4 cm, thickness 2.2 mm); a) Front view with the analyzed area A (white sqaure). b) Back view.

Fig. 5. (a) The acoustic micrograph in Fig. 4a. Regions marked by the white rectangles and enumerated as 1, 2 and 3 were selected for the $V(z)$ analysis. (b) The corresponding $V(z)$ curves for the areas in (a). The top panel corresponds to area 1, middle panel corresponds to area 2, and the bottom panel corresponds to area 3.

Areas of weld lines were reported in the literature to have reduced mechanical properties, as investigated for polymers with different filler nanoparticles using x-ray diffraction and scanning calorimetry (Xie and Ziegmann, 2011). A significant decrease in the tensile strength and impact properties in weld lines was also realized in scanning electron microscopy measurements, and was related to unfavorable fiber orientation beside the weld lines (Solymossy and Kovács, 2008). The flow induced molecular orientations were found to be different close to the weld line than they are away from the line (Nguyen-Chung, 2004). High likely the orientation at areas close to the weld lines is not parallel to

the residual stress leading to lower stifness (Darlington and Upperton, 1986). The residual stresses known to be anisotropic (Prime, 2017), were reported to have a complicated spatial distribution in welds and accordingly the velocity of surface acoustic waves varies close to a weld line than a way from it (acoustoelastic effect) (Park et al., 2014).

We next carried out THz imaging to verify the SAM results. Fig. 7 shows a THz C-scan in which the contrast mechanism is the arrival time of the echo from the top air/ABS interface, thus providing a map of the surface morphology. Later arrival time indicates the V-shaped groove associated with the weld evident in the image. The width is 400 μm and
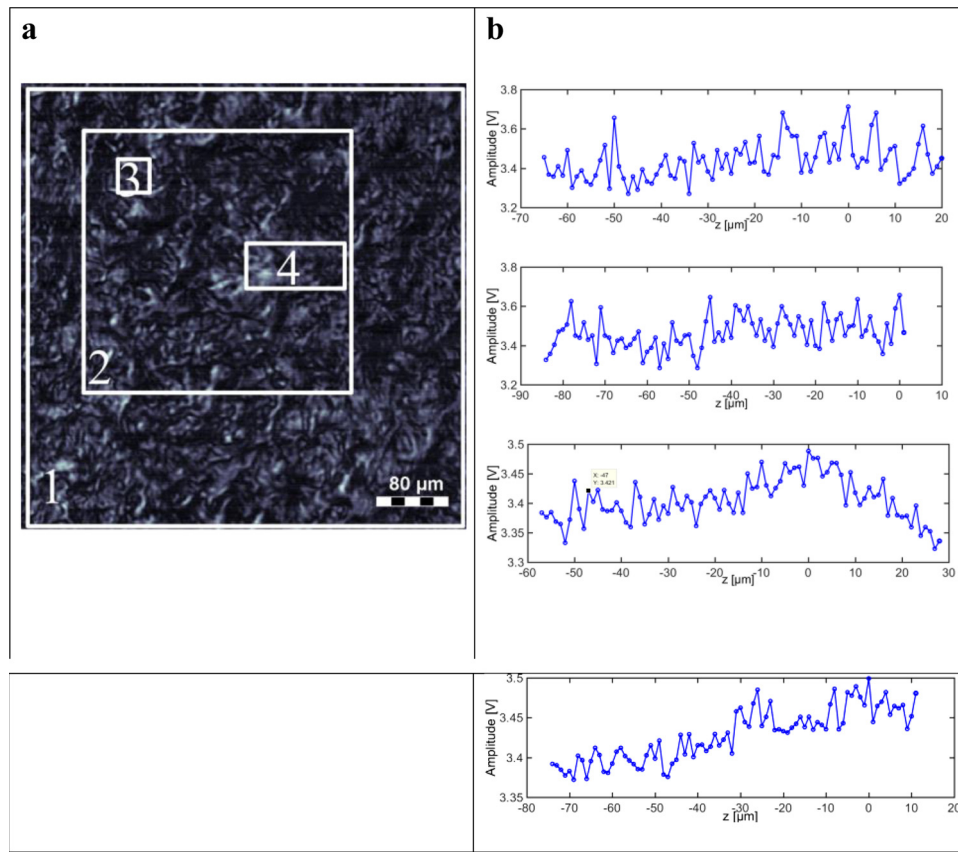
Fig. 6. a) The acoustic micrograph in Fig. 4b. Regions marked by the white rectangles and enumerated as 1, 2, 3 and 4 were selected for the V(z) analysis. (b) The corresponding V(z) curves for the areas in (a). The top panel corresponds to area 1, middle panel corresponds to area 2, and the bottom panel corresponds to area 3.

Table 1

V_R computed from the V(z) curves generated for the regions located at a distance of 2 mm right to the wild line as in Fig. 5a and for the regions located at a distance of 3.5 mm right to the wild line as in Fig. 6a.

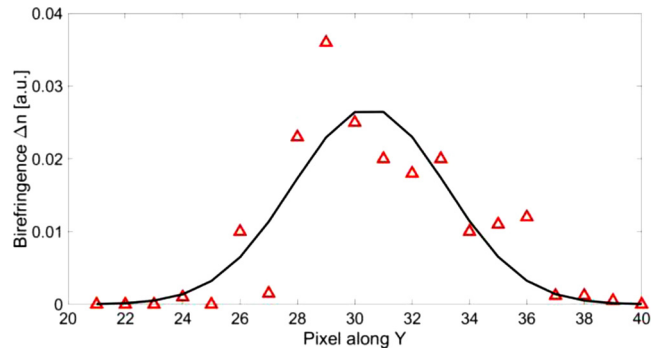| 2 mm right to wild line		3.5 mm left to wild line	
Region	V_R (m/s)	Region	V_R (m/s)
1	1543 ± 28	1	1625 ± 30
2	1527 ± 27	2	1633 ± 30
3	1537 ± 28	3	1625 ± 30
		4	1614 ± 29
Average	1535 ± 27		1624 ± 29

Fig. 8. Birefringence Δn is the difference in the refractive index for polarization along the extraordinary axis minus that for the ordinary axis. The figure shows line scan of Δn perpendicular to weld line in region A. The maximum value of Δn occurs at the weld line indicating local enhancement of molecular orientation parallel to the line and frozen-in anisotropic stress. The birefringence decays over a lengthscale of ˜1 mm away from the weld. Each pixel corresponds to a 200 μm spatial step. Birefringence falls off toward the background value on the 1-mm scale from the weld line.
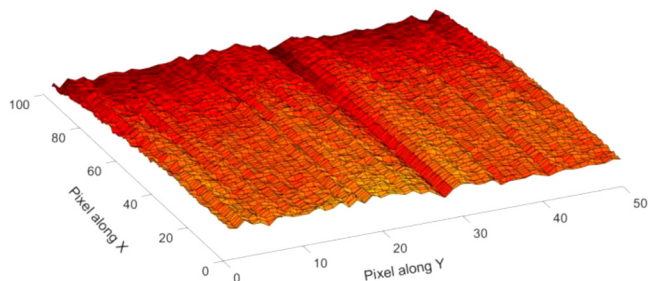

Fig. 7. THz image of region A. The contrast mechanism employed is the arrival time of the reflected pulse from the top air/ABS interface to provide a mapping of the surface morphology. The V-shaped groove corresponds to a region where the reflected pulse arrivers at a later time than the sourrounding regions. Groove width is 400 μm and depth 10 μm. Note that the transverse reolution of the mage is ˜ 200 μm.

the depth 10 μm. The width is close to the value obtained by SAM considering that the transverse resolution of the THz image is ˜ 200 μm. In Fig. 8 is plotted the birefringence Δn along a section perpendicular to the weld obtained from polarization-resolved reflective measurements. A knowledge of the plate thickness (measured with calipers) and the time delay between the pulse reflected from the top air/ABS interface and from the back ABS/air interface as a function of polarization provides Δn. Note the birefringence falls off on the (scale 1 mm away) from the weld line. This is somewhat larger than the width of the surface morphological feature (V-shaped groove) and indicates that frozen-in

strain and/or molecular orientation anisotropy extends somewhat further away from the weld than the morphological feature.

3. Conclusions

The deployment of many promising materials has been hampered by poor strength at certain locations. Specifically, injection-mold lines are often associated with poor mechanical strength. In this study, we apply the technique of SAW to explore the acoustic properties near injection-weld lines by comparing the velocity of (V_R) in locations close to and locations distant from the weld lines. We realize a considerable discrepancy in the V_R, indicating that the elastic moduli are much lower close to the weldline than distant from the weldlines and indicate anisotropic propagation. Beside the mechanical weakness close to weldlines, the microstructures visualized based on the micro-elastic contrasts indicate heterogeneity of the surface.

Comparisons were also made with THz imaging. Time-of-flight measurements indicate a V-shaped groove of width 400 μm and depth 10 μm. This width is in good agreement with the SAM measurements. We then characterized THz birefringence as a function of distance from the weld and find enhanced birefringence at the weld falling off to a background value over the 1-mm scale from the weld. This indicates that frozen-in strain and/or molecular anisotropy extends further from the weld than is indicated by the width of the V-shaped groove. In conclusion, SAM, in conjunction with THz birefringence imaging, may serve as a useful quality control combination to characterize local mechanical properties in a range of materials conducive to these techniques.

Declaration of competing interest

The authors declare that they have no known competing financial interests or personal relationships that could have appeared to influence the work reported in this paper.

Data availability

The raw/processed data required to reproduce these findings cannot be shared at this time due to technical limitations related to our Coronavirus lock-down.

Funding

Appendix A. Supplementary data

Supplementary material related to this article can be found, in the online version, at doi:https://doi.org/10.1016/j.micron.2020.102925.

References

Agassant, J., Mackley, M.R., 2016. Principles of polymer processing modelling. NUMIFORM 11002. https://doi.org/10.1051/matecconf/20168011002.

Ahmed Mohamed, E., Declercq, N., 2020. Giga-Hertz ultrasonic microscopy: Getting over the obscurity-A short review on the biomedical applications. Med. Phys. 9, 100025. https://doi.org/10.1016/j.phmed.2020.100025.

Ahmed Mohamed, E.T., Perone, J., Brand, S., Koegel, M., Nico, F., 2018. Scanning acoustic microscopy comparison of descemet′ s membrane normal tissue and tissue with Fuchs' endothelial dystrophy. Invest. Ophthalmol. Vis. Sci. 59 (13), 5627–5632.

Benak, A., 2019. Understanding water ingress in scanning acoustic microscopy and a method to observe defects that are open to the surface. ISTFA Conference Proceedings.

Bociaga, E., 2000. The effect of mold temperature and injection velocity on selected properties of polyethylene moldings. Polimery 45 (11/12), 830–836. https://doi.org/10.14314/polimery.2000.830.

Briggs, A., 1992. Acoustic microscopy-a summary. Rep. Prog. Phys. 55 (7), 851–909.

Chen, Z., Turng, L.S., 2005. A review of current developments in process and quality control for injection molding. Adv. Polym. Technol. 24 (3), 165–182. https://doi.org/10.1002/adv.20046.

da Fonseca, R.J.M., Ferdj-Allah, L., Despaux, G., Boudour, A., Robert, L., Attal, J., 1993. Scanning Acoustic Microscopy - Recent applications in materials science. Adv. Mater. 5 (7), 508–519.

Darlington, M.W., Upperton, P.H., 1986. Mechanical Properties of Reinforced Thermoplastics. Elsevier, London.

Demirkan, I., Yaprak, G., Ceylan, C., et al., 2020. Acoustic diagnosis of elastic properties of human tooth by 320 MHz scanning acoustic microscopy after radiotherapy treatment for head and neck cancer. Radiat. Oncol. 5 (38), 1–10. https://doi.org/10.1186/s13014-020-01486-7.

Dong, J., Locquet, A., Melis, M., Citrin, D.S., 2017. Global mapping of stratigraphy of an old-master painting using sparsity-based terahertz reflectometry. Sci. Rep. 7 (1), 1–12. https://doi.org/10.1038/s41598-017-15069-2.

Fu, G., Loh, N.H., Tor, S.B., Murakoshi, Y., Maeda, R., 2005. Effects of Injection Molding Parameters on the Production of Microstructures by Micropowder Injection Molding. Mater. Manuf. Process 20 (6).

Ghosh, S., Viana, J.C., Reis, R.L., Mano, J.F., 2007. Effect of processing conditions on morphology and mechanical properties of injection-molded poly(l-lactic acid). Polym. Eng. Sci. 47 (7), 1141–1147. https://doi.org/10.1002/pen.20799.

Gremaud, G., 2001. 9.4 scanning acoustic microscopy: SAM. Mater. Sci. Forum 366–368 (January 2001) pp. 676–0.

Heidari, B.S., Moghaddam, A.H., Davachi, S.M., Khamani, S., Alihosseini, A., 2019. Optimization of process parameters in plastic injection molding for minimizing the volumetric shrinkage and warpage using radial basis function (RBF) coupled with the k-fold cross validation technique. J. Polym. Eng. 39 (5), 481–492. https://doi.org/10.1515/polyeng-2018-0359.

Hopmann, C., Wipperfürth, J., 2017. Ultrasound tomography for spatially resolved melt temperature masurements in injection moulding processes. J. Appl. Mech. Eng. 06 (03). https://doi.org/10.4172/2168-9873.1000264.

Kulich, D.M., Gaggar, S.K., Lowry, V., Stepien, R., 2002. Acrylonitrile–Butadiene–Styrene polymers. In: Mark, H. (Ed.), Encyclopedia of Polymer Science and Technology. John Wiley & Sons, Inc. https://doi.org/10.1002/0471238961.01021911211209.a01.pub2.

Li, M., Feng, Z., 2016. Accurate Young's modulus measurement based on Rayleigh wave velocity and empirical Poisson's ratio. Rev. Sci. Instrum. 87 (7).

Mistretta, M.C., Botta, L., Morreale, M., Rifici, S., Ceraulo, M., La Mantia, F.P., 2018. Injection molding and mechanical properties of bio-based polymer nanocomposites. Materials (Basel) 11 (4), 1–14. https://doi.org/10.3390/ma11040613.

Mohan, M., Ansari, M.N.M., Shanks, R.A., 2017. Review on the effects of process parameters on strength, shrinkage, and sarpage of injection molding plastic component. Polym. Technol. Eng. 56 (1), 1–12.

Nasić, E., Šarić, E., Halilović, J., Džemal, K., 2018. Effect of injection molding parameters on wild line tensile. J. Trends Dev. Mach. 21 (1), 13–16.

Nguyen-Chung, T., 2004. Flow analysis of the weld line formation during injection mold filling of thermoplastics. Rheol. Acta 43 (3), 240–245.

Oh, G., Jeong, J., Park, S., Kim, H., 2018. Terahertz time-domain spectroscopy of weld line defects formed during an injection moulding process. J. Compos. Mater. 157, 67–77. https://doi.org/10.1016/j.compscitech.2018.01.030.

Park, I.-K., Yoshida, S., Didie, D., Ghimire, S., 2014. Simultanous application of acoustic and optical tecchniques to non-destructive evaluation. In: Jin, H., Sciammarella, C., Yoshida, S., Lamberti, L. (Eds.), Advancement of Optical Methods in Experimental Mechanics. Springer, New York pp. 139–139.

Passini, A., Capella, A., Oliveira, D., Riva, R., 2011. Ultrasonic inspection of AA6013 laser welded joints. Mater. Res. 14 (3), 417–422.

Prime, M.B., 2017. Amplified effect of mild plastic anisotropy on residual stress. Int. J. Solids Struct. 118–119, 70–77.

Rizvi, S.J.A., 2017. Effect of injection molding parameters on crystallinity and mechanical properties of isotactic polypropylene. Int. J. Plast. Technol. 21 (2), 404–426. https://doi.org/10.1007/s12588-017-9194-3.

SJ, L., et al., 2004. Optimization process conditions of shrinkage and warpage of thin-wall parts. Polym. Eng. Sci. 44 (5), 917–928. https://doi.org/10.1002/pen.20083.

Solymossy, B., Kovács, J.G., 2008. The examination of weld line properties in injection molded PP Composites. Mater. Sci. Forum 589, 263–267.

Tittmann, B.R., Kessler, L.W., 2018. Acoustic microscopy. In: In: Ahmad, Q., Bond, L.J. (Eds.), Non-Destructive Evaluation of Materials, volume 17. Digital library, pp. 331–352.

Weiglein, R.G., Wilson, R.D., 1978. Characteristic material signatures by acoustic microscopy. Electron. Lett. 14 (12), 352–354.

Xie, L., Ziegmann, G., 2011. Mechanical properties of the weld line defect in micro injection molding for various nano filled polypropylene composites. J. Alloys. Compd. 509 (2), 226–233.

Yu, Z., Boseck, S., 1995. Scanning acoustic microscopy and its applications to material characterization. Rev. Mod. Phys. 67 (4), 863–891.